Flat-band-induced itinerant ferromagnetism in RbCo$_2$Se$_2$

Jianwei Huang,[1] Zhicai Wang,[2] Hongsheng Pang,[2] Han Wu,[1] Huibo Cao,[3] Sung-Kwan Mo [●],[4] Avinash Rustagi [●],[5,6]
A. F. Kemper [●],[5] Meng Wang [●],[7,8,*] Ming Yi [●],[1,8,†] and R. J. Birgeneau[8,9,‡]

[1]*Department of Physics and Astronomy, Rice University, Houston, Texas 77005, USA*
[2]*School of the Gifted Young, University of Science and Technology of China, Hefei, Anhui 230026, China*
[3]*Neutron Scattering Division, Oak Ridge National Laboratory, Oak Ridge, Tennessee 37831, USA*
[4]*Advanced Light Source, Lawrence Berkeley National Laboratory, Berkeley, California 94720, USA*
[5]*Department of Physics, North Carolina State University, Raleigh, North Carolina 27695, USA*
[6]*School of Electrical and Computer Engineering, Purdue University, West Lafayette, Indiana 47907, USA*
[7]*School of Physics, Sun Yat-Sen University, Guangzhou, Guangdong 510275, China*
[8]*Department of Physics, University of California, Berkeley, California 94720, USA*
[9]*Materials Science Division, Lawrence Berkeley National Laboratory, Berkeley, California 94720, USA*

ACo$_2$Se$_2$ (A=K, Rb, Cs) is a homologue of the iron-based superconductor AFe$_2$Se$_2$. From a comprehensive study of RbCo$_2$Se$_2$ via measurements of magnetization, transport, neutron diffraction, angle-resolved photoemission spectroscopy, and first-principles calculations, we identify a ferromagnetic order accompanied by an orbital-dependent spin splitting of the electronic dispersions. Furthermore, we identify the ordered moment to be dominated by a $d_{x^2-y^2}$ flat band near the Fermi level, which exhibits the largest spin splitting across the ferromagnetic transition, suggesting an itinerant origin of the ferromagnetism. In the broader context of the iron-based superconductors, we find this $d_{x^2-y^2}$ flat band to be a common feature in the band structures of both iron chalcogenides and iron pnictides, accessible via heavy electron doping.

I. INTRODUCTION

The parent compounds of most iron-based superconductors (FeSCs) are collinear antiferromagnetic (AFM) metals [1], with nearly compensated hole and electron Fermi pockets separated by the AFM wave vector [2]. Superconductivity emerges with the suppression of the AFM order [3]. In the intercalated iron chalcogenides, A_xFe$_{2-\delta}$Se$_2$ (A=K, Rb, Cs), parent compounds typically exhibit insulating behaviors with a variety of AFM orders [4,5]. By tuning the iron content, one can achieve iron vacancy-free superconducting phases in A_xFe$_2$Se$_2$ (A=K, Rb, Cs) [6], which exhibit large electron Fermi pockets near the Brillouin zone (BZ) corners.

ACo$_2$Se$_2$ (A=K, Rb, Cs) is an isostructural homologue of the vacancy-free superconducting AFe$_2$Se$_2$ phase with Fe substituted by Co [7], albeit with distinct physical properties. While AFe$_2$Se$_2$ is a superconductor with an AFM insulating parent phase [4–6], ACo$_2$Se$_2$ exhibits metallic magnetic ground states without superconductivity. In particular, ACo$_2$Se$_2$ consists of planar ferromagnetic (FM) sheets that are either aligned (KCo$_2$Se$_2$ and RbCo$_2$Se$_2$) or antialigned (A-type AFM in CsCo$_2$Se$_2$) [7–10]. Due to the metallicity, an itinerant nature has been proposed as the origin of the magnetism [8,11]. In such a scenario, band splitting into the spin-majority and spin-minority bands is expected [12–14]. However, while the low-temperature electronic structure of KCo$_2$Se$_2$ has been measured [15], no direct observation of electronic reconstruction across the FM transition has been reported for this series of itinerant magnets.

Here we report the evolution of the electronic structure of RbCo$_2$Se$_2$ across the FM transition via angle-resolved photoemission spectroscopy (ARPES), together with characterization by magnetization, transport, and neutron diffraction measurements. We identify a nearly flat band near the Fermi level E_F that exhibits the largest splitting in the FM phase. From first-principles calculations, we identify this band to be a $d_{x^2-y^2}$ flat band that contributes the most to the density of states at E_F and therefore drives the itinerant FM in this material. Furthermore, in the larger context of the FeSCs, we find this $d_{x^2-y^2}$ flat band to be a common feature in the calculated band structures in both the FeSe-based and FeAs-based systems that is accessible via heavy electron doping. Combining the phenomenology across the FeSC families, we point out a connection between the emergence of various symmetry-breaking phases and the common features in the low-energy Fe 3d bands tunable via carrier doping.

II. METHODS

Single crystals of RbCo$_2$Se$_2$ were grown by the self-flux method [9]. High-purity Rb, Co, and Se were used as the starting materials and prepared in the ratio of 1:2:2. Sample magnetization and resistivity were measured with a

*wangmeng5@mail.sysu.edu.cn
†mingyi@rice.edu
‡robertjb@berkeley.edu

commercial Magnetic Property Measuring System and Physical Property Measurement System. Neutron diffraction was carried out on the HB3A four-circle diffractometer at the High Flux Isotope Reactor, Oak Ridge National Laboratory, with a neutron wavelength of $\lambda = 1.553$ Å selected by a bent perfect Si-220 monochromator [16]. The nuclear and magnetic structures were refined with the FULLPROF suite [17], resulting in a refined stoichiometry of $Rb_{0.93}Co_{1.87}Se_2$ and lattice constants $a = 3.870$ Å and $c = 13.876$ Å. ARPES measurements were carried out at beamline 10.0.1 of the Advanced Light Source with a Scienta R4000 hemispherical energy analyzer. The energy resolution was set as 12.5 meV, and the angular resolution was set as $0.3°$. The photon energy of the light was set at 45 eV in an s-polarization geometry where the polarization vector was perpendicular to the electron analyzer slit. The samples were cleaved *in-situ* at 30 K and kept in ultrahigh vacuum with a base pressure better than 3×10^{-11} Torr during measurements.

The electronic structure calculations were performed using density functional theory (DFT) via QUANTUM ESPRESSO [18,19] with plane wave scalar relativistic pseudopotentials. The exchange-correlation energy was described by the generalized gradient approximation in the scheme proposed by Perdew, Burke, and Ernzerhof [20] with a wave function cutoff energy of 40 Ry. The BZ was sampled for integration according to the scheme proposed by Monkhorst and Pack [21] with a grid of $10 \times 10 \times 10$ k points. Experimentally determined lattice constants were used with the out-of-plane Se atomic locations determined from relaxing the system. Calculations were performed for both the nonmagnetic and FM cases, where the total magnetization per unit cell was constrained to match that of the experimental value.

III. RESULTS

The crystal and magnetic structures of $RbCo_2Se_2$ are shown in Fig. 1(a). The ordered magnetic moment is determined from neutron diffraction to be $0.60(4)\mu_B$ per Co site aligned along the a axis, consistent with previous reports [7,9]. Magnetization measurement with the magnetic field in the ab plane identifies an onset of the FM order at $T_c = 83$ K [Fig. 1(c)]. A hysteresis behavior confirming the FM ground state is observed at 2 K as a function of external field [Fig. 1(d)]. A kink at T_c can also be identified in the resistance measurement [Fig. 1(e)]. Finally, the integrated counts at the (0,0,4) magnetic Bragg peak from our neutron diffraction measurements clearly confirm the FM transition at T_c [Fig. 1(f)].

Having confirmed the FM transition, we present the measured electronic structure in the paramagnetic phase. At 150 K $> T_c$, the Fermi surfaces (FSs) of $RbCo_2Se_2$ exhibit one small electron pocket (γ) around the BZ center, Γ, and three electron pockets around the BZ corner, X [Fig. 2(a)]. To show better contrast, we present the raw data in the upper half of the FS and its two-dimensional (2D) curvature images in the bottom half. We note that the X_1 and X_2 points as labeled are equivalent under C_4 rotational symmetry of the tetragonal crystal structure. However, the map intensity appears different here due to the usage of linear horizontal polarization, which probes the d_{xz} and d_{yz} orbitals differently due to
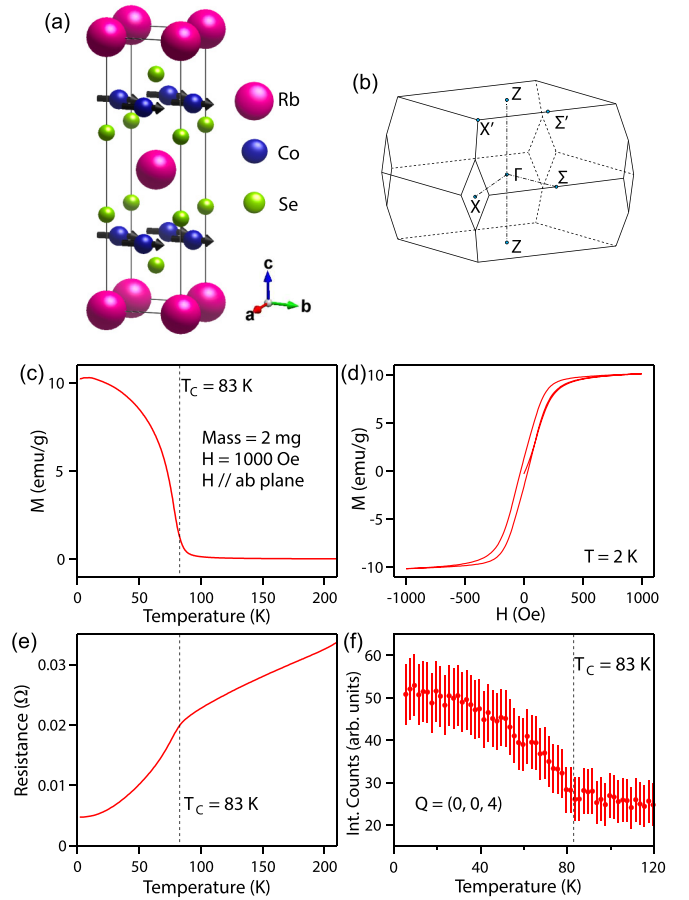

FIG. 1. FM characterization. (a) Crystal and magnetic structure of $RbCo_2Se_2$ with magnetic moments indicated by arrows. (b) BZ notations. (c) Temperature-dependent magnetization at 1000-Oe external magnetic field. (d) Field-dependent magnetization at 2 K. (e) Resistance as a function of temperature. (f) Neutron diffraction measurements of the integrated intensity of the (0,0,4) magnetic Bragg peak as a function of temperature.

photoemission matrix element effects [22]. A large electron pocket (α) around X_1 is easy to discern [Fig. 2(a)]. The presence of a second weaker inner electron band (β) is evident both from the FS images at X_1 and from the momentum-distribution curve (MDC) taken from E_F, which can be fitted with four Lorentzian peaks on a constant background [Fig. 2(b)]. A third electron band (ε) can be observed at the X_2 point due to the distinct matrix element effect for the two equivalent X points [Fig. 1(a)] [22]. Its fitted k_F points (Fermi momenta) are plotted in Fig. 2(a), which are distinct from those of the α and β electron bands, confirming a total of three electron pockets at the X point. The identification of their dominant orbital character and expected matrix element effects will be discussed in a later section. Compared with the iron chalcogenide superconductors AFe_2Se_2, the electron pockets of $RbCo_2Se_2$ at the X point are much larger, consistent with additional electron doping provided by the substitution of Fe by Co [23,24].

In comparison, the number of FS sheets observed deep in the FM phase increases. Most notable is the splitting of the α FS at X_1 [Fig. 2(c)]. This is evident from both the FS map in
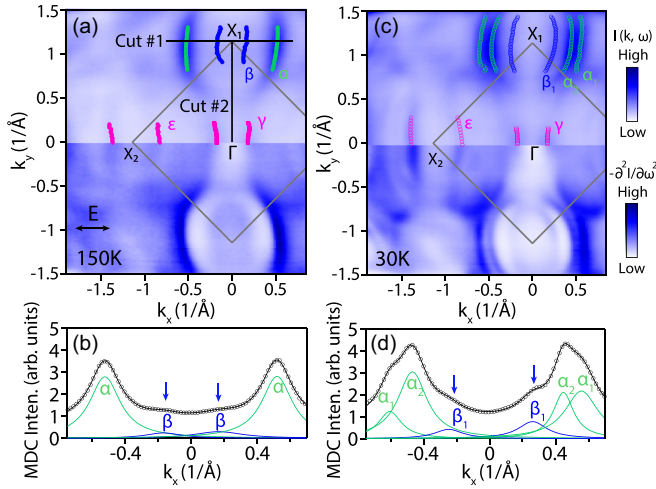
FIG. 2. Fermi surfaces across T_c. (a) FS mapping at 150 K > T_c. The $k_y > 0$ ($k_y < 0$) region shows the raw data (2D curvature). Markers indicate MDC-fitted FSs. (b) MDC at E_F along cut 1 in (a) fitted with four Lorentzians and a constant background. The blue arrows indicate the β band. (c) and (d) Same as (a) and (b), except taken at 30 K in the FM state.

Fig. 2(c) and a comparison of the MDCs across X_1 [Fig. 2(d)], which can now be fitted with six Lorentzian peaks showing a splitting of the peak previously identified as the α pocket at 150 K. This is consistent with a band splitting due to the FM ordering. We therefore label these the α_1 and α_2 pockets, which correspond to the spin-majority and spin-minority bands, respectively. The k_F opening (defined by the separation in momentum) of the pair of peaks labeled β_1 has expanded compared to that of the β pocket in the paramagnetic phase, suggesting that the pair observed at 30 K is likely the spin-majority branch of the β band that has shifted downwards in energy while the spin-minority β_2 band has shifted to above E_F and hence is not observed. In contrast, we do not observe obvious shifts of the electron pocket (γ) at Γ and the electron pocket (ε) at X_2 below T_c [Figs. 2(a) and 2(b)].

The spin splitting of bands in the presence of the FM order can be further visualized from the band dispersions. Band images measured across X_1 in the paramagnetic phase (150 K) are shown in Fig. 3(a). Related band dispersions obtained by MDC fitting as well as the k_F positions of the ε electron pocket are overlaid on the image. To understand better the observed bands, we have performed DFT calculations of non-magnetic and FM states of RbCo$_2$Se$_2$. Focusing around the X point in the paramagnetic phase [Fig. 3(d)], our observed dispersions show reasonable comparison with the calculated electron bands, where a total of three electron bands appear near E_F. From the size of the k_F openings, the outermost band and the innermost band (solid black bands) likely correspond to the α and β bands observed at X_1, while the middle band (dotted black band) corresponds to the ε band observed at X_2 [Fig. 2(a)]. This assignment is further supported by a consideration of the orbital characters of these bands and the photoemission matrix element effects, as will be discussed shortly. To match with the Fermi velocity of the outermost α band, a renormalization factor of 2.9 is applied to the DFT calculations, suggesting moderate electronic correlations in
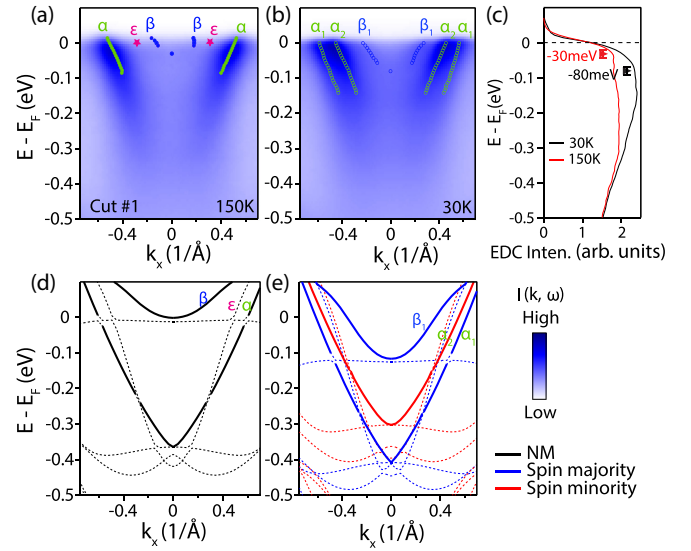

FIG. 3. Electronic structure across T_c. (a) Spectral image along cut 1 in Fig. 2(a) with MDC-fitted dispersions. The k_F value of ε is obtained from fitting the MDC at the equivalent X_2 point. (b) Same as (a), except taken at 30 K in the FM state. (c) Energy distribution curves (EDCs) at the X_1 point. The markers indicate the β band bottom obtained by fitting the corresponding data points in (a) and (b) with a parabolic curve. Fitting uncertainty gives a ±10-meV error bar. (d) DFT band calculations in the paramagnetic phase renormalized by a factor of 2.9. (e) Same as (d), except in the FM state.

RbCo$_2$Se$_2$. We also note that there exists an orbital-dependent relative shift that would be needed to match the calculations. Such behavior has been commonly observed in iron-based superconductors [25–27].

In the FM state [Fig. 3(b)], the α band is observed to split into two bands, i.e., α_1 and α_2. The β band is observed to shift down in energy compared to that in the paramagnetic phase. In the calculated band structure in the FM state [Fig. 3(e)], the α band splits into the spin-majority band and spin-minority band, marked by solid blue and red curves. Similarly, the β band also splits with the spin-majority band shifted down, while the spin-minority band has shifted to well above E_F. The bottom of the β band is observed to be at 30 meV below E_F in the paramagnetic state, while the spin-majority band is shifted down to 80 meV below E_F in the FM state [Fig. 3(c)]. An estimation based on the assumption of equal spin splitting therefore locates the spin-minority band of β at 20 meV above E_F, and hence, it is not observed.

Furthermore, we observe a nearly flat band from the spectra image at cut 2 along the Γ-X direction [Fig. 4(a)]. The flat band sits close to E_F at 150 K in the paramagnetic state. It splits into two at 30 K in the FM state, as is evident in the comparison of the energy distribution curve (EDC) stacks between 30 and 150 K, where a single peak at 150 K splits into a peak at lower energy with a shoulder near E_F at 30 K, which is likely the residual tail of the spin-minority band that has shifted above E_F [Fig. 4(c)]. The band-splitting behavior of this flat band is reminiscent of that of the β band, where the spin-majority band is shifted down below E_F while the spin-minority band shifts above E_F. The diminishing of the
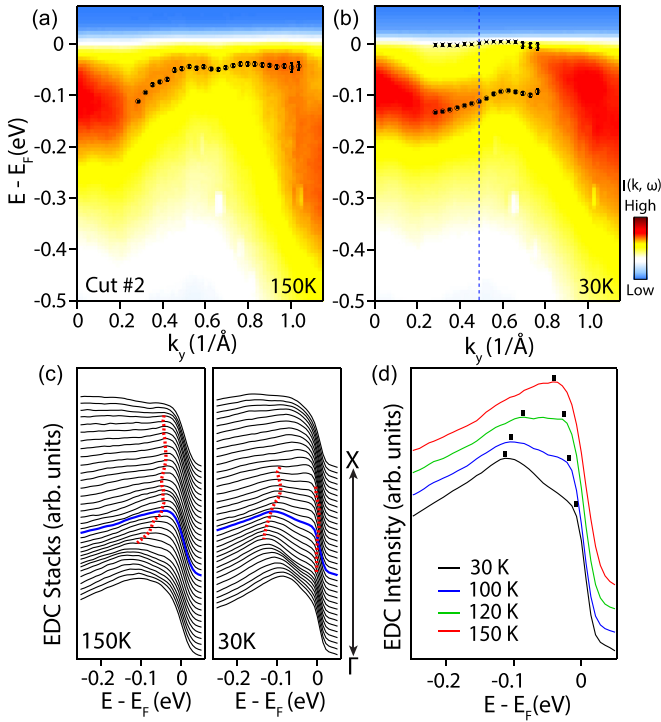
FIG. 4. Flat band across T_c. (a) and (b) Spectra images along cut 2 in Fig. 2(a) at 150 and 30 K, respectively. Markers are the corresponding fitted peak positions in (c). (c) EDC stacks of (a) and (b). Red markers indicated peak positions from fitting the EDCs with two Lorentzians and a constant background multiplied by the Fermi-Dirac function. (d) Temperature-dependent EDCs at the momentum indicated by the blue dashed line in (b).
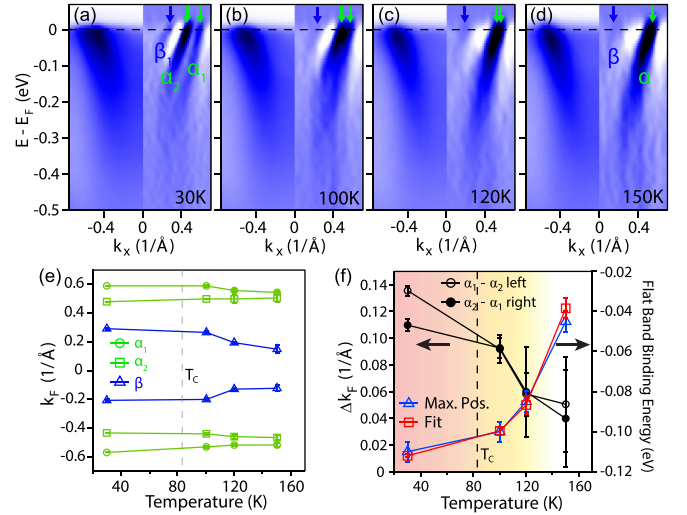

FIG. 5. Temperature dependence of band splittings. (a)–(d) Temperature-dependent spectra along cut 1 marked in Fig. 2(a). The left (right) half shows the raw data (second momentum derivative). (e) Fitted k_F of α_1, α_2, and β_1 bands as a function of temperature. Error bars are obtained from the fitting uncertainty. (f) Temperature dependence of α-band Δk_F and the shift of the flat band from fitting the peak position in the EDCs and maximum positions in Fig. 4(d).

flat band splitting with increasing temperature is shown by EDCs at different temperatures in Fig. 4(d).

To confirm further the relation between the band splitting and the FM order, we examine the evolution of the spin splitting with temperature. With increasing temperature, the α_1 and α_2 bands are observed to merge [Figs. 5(a)–5(d)]. However, they remain split at 100 K. To quantify the splitting against temperature, we extract k_F of the α and β bands by fitting the MDC at E_F [Fig. 5(e)], from which we can also extract the k_F differences [Fig. 5(f)]. In addition, the splitting of the flat band can also be tracked from the peaks in the EDCs [Fig. 4(d)]. Our observation of the bands splitting versus temperature shows that while spin splitting of bands occurs across T_c, the onset of the splittings persists to a higher temperature than T_c, suggestive of ferromagnetic fluctuations in the paramagnetic state.

To understand better the behavior of the band-dependent splitting, we carried out orbital-projected DFT calculations of both nonmagnetic and FM RbCo$_2$Se$_2$. From the nonmagnetic calculations, three electron bands appear around the X point [Fig. 6(b)], the relative sizes of which allow us to identify the observed α, β, and ε bands as the calculated bands with dominantly $d_{xz/yz}$, $d_{x^2-y^2}$, and d_{xy} orbital characters, respectively. This assignment is consistent with the expected photoemission matrix element effects, where under the s polarization used, the α (d_{xz}/d_{yz}) band shows strong intensity at the X_1 point due to its odd symmetry with respect to the Γ-X direc-

tion, while the ε (d_{xy}) band exhibits observable but weaker intensity at the X_2 point due to switched parity under the glide mirror symmetry [28]. The innermost β band is usually not observable in FeSC parent compounds due to its high kinetic energy but is now observable due to the heavy electron doping from Co. We find a qualitative match between the calculated and measured dispersions with a renormalization factor of 2.9 to match the Fermi velocity of the observed α band [Fig. 3(a)]. We also note that the γ band is a highly k_z dispersive band,
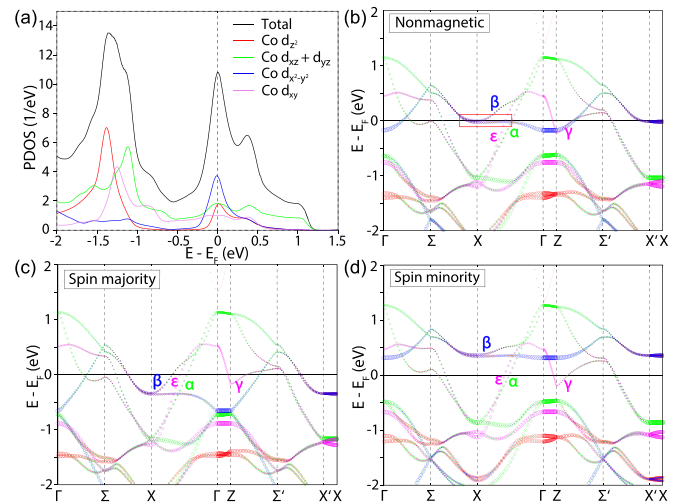

FIG. 6. Calculated electronic structures. (a) Calculated PDOS projected onto Co d orbitals in the nonmagnetic state. (b)–(d) Calculated orbital-resolved band dispersion in the nonmagnetic, spin-majority, and spin-minority states, respectively. The marker size represents the spectral weight.

TABLE I. Orbital-resolved contribution of the magnetic moment from the Co $3d$ orbitals, with a total of $0.60(4)\mu_B$ per Co from all orbitals.

Orbital	$d_{x^2-y^2}$	$d_{xz/yz}$	d_{xy}	d_{z^2}
Magnetic moment (in units of μ_B)	0.30	0.10	0.02	0.11

where its band bottom is below E_F near Z and rises to above E_F near Γ. Since we do observe the γ electron band at the BZ center, we are likely measuring near $k_z = \pi$. Importantly, a flat band appears at E_F in the nonmagnetic calculation along Γ-X with dominant $d_{x^2-y^2}$ orbital character, consistent with our ARPES measurements [Fig. 4(a)]. Such a flat band leads to a large density of states (DOS) at E_F, which could induce a strong FS instability, resulting in a band splitting—the spin-majority band and spin-minority band—to reduce the overall energy of the system [11,29].

Indeed, a large DOS at E_F is contributed by this flat band, as seen from the calculated orbital-projected DOS for the non-magnetic phase [Fig. 6(a)]. In the calculation for the FM state, the spin splitting between the majority and minority bands is orbital dependent: largest in the $d_{x^2-y^2}$ flat band, followed by the $d_{xz/yz}$ bands and, finally, the d_{xy} bands [Figs. 6(c) and 6(d)]. This orbital-dependent band splitting is consistent with our ARPES measurements in that the splittings of the flat band and the α and β bands are clearly observed, while those of the ε band are not. Similarly, the γ electron band observed at Γ is also dominantly of d_{xy} character, where no significant modification across T_c is observed [Figs. 2(a) and 2(c)]. We can confirm further the role of the $d_{x^2-y^2}$ flat band in the itinerant ferromagnet by calculating the contribution to the ordered moment from different orbitals (Table I). Indeed, the $d_{x^2-y^2}$ orbital contributes $0.3\mu_B$ out of the $0.60(4)\mu_B$ total ordered magnetic moment per Co site (Table I), while the d_{xy} orbital contributes merely $0.02\mu_B$. Our combined experimental and theoretical results support a flat band-induced itinerant origin for the ferromagnetism in RbCo$_2$Se$_2$.

Finally, it is interesting to note that this $d_{x^2-y^2}$ flat band is a commonality in the electronic structure of FeSCs. Besides the ACo$_2$Se$_2$ family, SrCo$_2$As$_2$ was also recently identified to host itinerant ferromagnetism due to a flat band near E_F [30,31]. Taking the observed electronic phases together among FeSCs, we point out the following phenomenology in relation to the common electronic structure of the Fe $3d$ orbitals. We use band structure calculations for FeSe [32] and BaFe$_2$As$_2$ [33] to represent the FeSe-based and FeAs-based materials in which common features are highlighted [Figs. 7(a) and 7(b)]. We illustrate three main types of fermiologies observed. For the undoped parent compounds such as BaFe$_2$As$_2$, NaFeAs, LaFeAsO, and Fe(Te,Se), the chemical potential leads to quasinested hole pockets at the BZ center and electron pockets at the BZ corner, where a collinear spin density wave (SDW) appears at the nesting wave vector with the associated nematic order [Fig. 7(c)] [25,27,34–38]. Superconductivity appears when these competing orders are suppressed with doping or chemical pressure. With further heavy electron doping, the chemical potential shifts up [green line in Fig. 7(a) and 7(b)] such that the hole bands
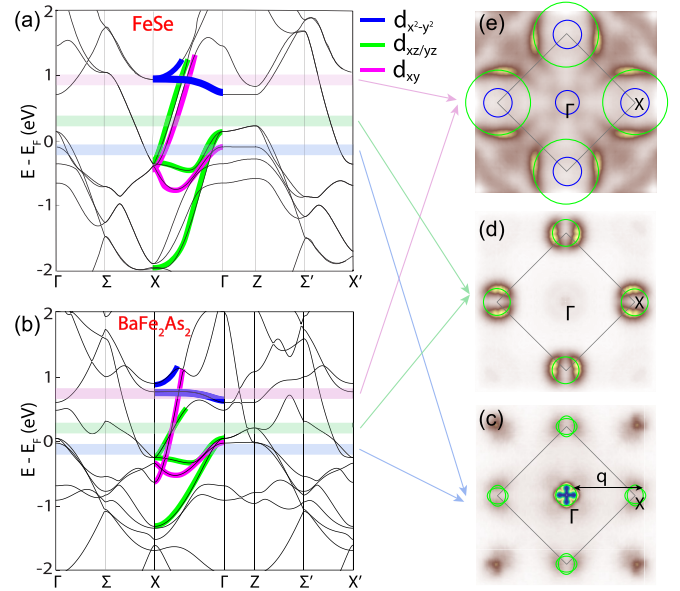

FIG. 7. Electronic phases in iron-based superconductors. (a) and (b) Band structure calculations of FeSe [32] and BaFe$_2$As$_2$ [33]. Common features along Γ-X are highlighted by dominant orbitals. Horizontal lines represent different chemical potentials tunable via electron doping as exemplified by FSs of (c) Fe(Se,Te), (d) high-T_c RbFe$_2$Se$_2$, and (e) flat band itinerant FM RbCo$_2$Se$_2$.

at Γ sink below E_F, leaving enlarged electron pockets at the BZ corner, largely destroying the nesting condition. The group of materials exhibiting this type of fermiology includes the heavily electron doped iron chalcogenides such as AFe$_2$Se$_2$ [23,24,39], (Li,Fe)OHFeSe [40,41], and monolayer FeSe film grown on a SrTiO$_3$ substrate [42–45], exhibiting no competing ordered ground states and superconductivity appearing with T_c of 30 to 65 K. With further electron doping, as achieved by replacing Fe with Co, the chemical potential can be tuned further up [pink line in Figs. 7(a) and 7(b)], where the electron pockets at the zone corner are further enlarged. In this doping regime, a flat band appears near E_F, as has been identified in both SrCo$_2$As$_2$ and ACo$_2$Se$_2$, driving the electronic system into an itinerant ferromagnetic state [15,31,46–48]. It is interesting to point out that optimal superconductivity among FeSCs appears in the heavily electron doped iron chalcogenides in which the fermiology is farthest away from instabilities, leading to competing phases—on one side, the quasinesting inductive of SDW order and, on the other, the flat band inductive of itinerant ferromagnetism.

IV. CONCLUSION

To summarize, we reported the evolution of the electronic structure of the itinerant FM compound RbCo$_2$Se$_2$ across its FM transition. In the paramagnetic state, the much enlarged electron Fermi pockets around the BZ corner indicate the heavy electron doping from its superconducting isostructural analog RbFe$_2$Se$_2$. A renormalization factor of 2.9 suggests moderate electron-electron correlations, comparable with those in iron-based superconductors. We found an

orbital-dependent band splitting in the FM state. In comparison to first-principles calculations, we found our observations are consistent with a flat band itinerant origin of the ferromagnetism. Furthermore, the band splitting is observed to persist within a finite-temperature window above the FM transition, suggesting FM fluctuations above the long-range ordering temperature. Finally, we pointed out a phenomenological observation of the appearance of high-temperature superconductivity in iron-based superconductors bounded by competing phases of SDW and nematicity on one side in a quasinested fermiology and flat band itinerant ferromagnetism on the other side, tunable via carrier doping.

ACKNOWLEDGMENTS

[1] C. de la Cruz, Q. Huang, J. W. Lynn, J. Li, W. Ratcliff II, J. L. Zarestky, H. A. Mook, G. F. Chen, J. L. Luo, N. L. Wang, and P. Dai, Nature (London) **453**, 899 (2008).

[2] M. Yi, Y. Zhang, Z.-X. Shen, and D. Lu, npj Quantum Mater. **2**, 57 (2017).

[3] A. A. Kordyuk, Low Temp. Phys. **38**, 888 (2012).

[4] P. Dai, Rev. Mod. Phys. **87**, 855 (2015).

[5] M. Wang, M. Yi, H. Cao, C. de la Cruz, S. K. Mo, Q. Z. Huang, E. Bourret-Courchesne, P. Dai, D. H. Lee, Z. X. Shen, and R. J. Birgeneau, Phys. Rev. B **92**, 121101(R) (2015).

[6] M. Wang, M. Yi, W. Tian, E. Bourret-Courchesne, and R. J. Birgeneau, Phys. Rev. B **93**, 075155 (2016).

[7] G. Huan, M. Greenblatt, and M. Croft, Eur. J. Solid State Inorg. Chem. **26**, 193 (1989).

[8] G. Huan and M. Greenblatt, J. Less-Common Met. **156**, 247 (1989).

[9] J. Yang, B. Chen, H. Wang, Q. Mao, M. Imai, K. Yoshimura, and M. Fang, Phys. Rev. B **88**, 064406 (2013).

[10] F. von Rohr, A. Krzton-Maziopa, V. Pomjakushin, H. Grundmann, Z. Guguchia, W. Schnick, and A. Schilling, J. Phys.: Condens. Matter **28**, 276001 (2016).

[11] E. C. Stoner, Proc. R. Soc. London, Ser. A **165**, 372 (1938).

[12] H.-B. Yang, S.-C. Wang, A. K. P. Sekharan, H. Matsui, S. Souma, T. Sato, T. Takahashi, T. Takeuchi, J. C. Campuzano, R. Jin, B. C. Sales, D. Mandrus, Z. Wang, and H. Ding, Phys. Rev. Lett. **92**, 246403 (2004).

[13] M. Güttler *et al.*, Sci. Rep. **6**, 24254 (2016).

[14] F. Mazzola, V. Sunko, S. Khim, H. Rosner, P. Kushwaha, O. J. Clark, L. Bawden, I. Marković, T. K. Kim, M. Hoesch, A. P. Mackenzie, and P. D. C. King, Proc. Natl. Acad. Sci. USA **115**, 12956 (2018).

[15] Z. H. Liu, Y. G. Zhao, Y. Li, L. L. Jia, Y. P. Cai, S. Zhou, T. L. Xia, B. Büchner, S. V. Borisenko, and S. C. Wang, J. Phys.: Condens. Matter **27**, 295501 (2015).

[16] B. C. Chakoumakos, H. Cao, F. Ye, A. D. Stoica, M. Popovici, M. Sundaram, W. Zhou, J. S. Hicks, G. W. Lynn, and R. A. Riedel, J. Appl. Crystallogr. **44**, 655 (2011).

[17] J. Rodríguez-Carvajal, Phys. B (Amsterdam, Neth.) **192**, 55 (1993).

[18] P. Giannozzi *et al.*, J. Phys.: Condens. Matter **21**, 395502 (2009).

[19] P. Giannozzi *et al.*, J. Phys.: Condens. Matter **29**, 465901 (2017).

[20] We used the pseudopotentials RB.PBE-SP-HGH.UPF, CO.PBE-ND-RRKJUS.UPF, and SE.PBE-N-RRKJUS_PSL.0.2.UPF from the QUANTUM ESPRESSO pseudopotential database, http://www.quantum-espresso.org/pseudopotentials.

[21] H. J. Monkhorst and J. D. Pack, Phys. Rev. B **13**, 5188 (1976).

[22] M. Yi, D. Lu, J.-H. Chu, J. G. Analytis, A. P. Sorini, A. F. Kemper, B. Moritz, S.-K. Mo, R. G. Moore, M. Hashimoto, W.-S. Lee, Z. Hussain, T. P. Devereaux, I. R. Fisher, and Z.-X. Shen, Proc. Natl. Acad. Sci. USA **108**, 6878 (2011).

[23] D. Mou *et al.*, Phys. Rev. Lett. **106**, 107001 (2011).

[24] Y. Zhang, L. X. Yang, M. Xu, Z. R. Ye, F. Chen, C. He, H. C. Xu, J. Jiang, B. P. Xie, J. J. Ying, X. F. Wang, X. H. Chen, J. P. Hu, M. Matsunami, S. Kimura, and D. L. Feng, Nat. Mater. **10**, 273 (2011).

[25] M. Yi, D. H. Lu, J. G. Analytis, J.-H. Chu, S.-K. Mo, R.-H. He, R. G. Moore, X. J. Zhou, G. F. Chen, J. L. Luo, N. L. Wang, Z. Hussain, D. J. Singh, I. R. Fisher, and Z.-X. Shen, Phys. Rev. B **80**, 024515 (2009).

[26] V. Brouet, P.-H. Lin, Y. Texier, J. Bobroff, A. Taleb-Ibrahimi, P. Le Fèvre, F. Bertran, M. Casula, P. Werner, S. Biermann, F. Rullier-Albenque, A. Forget, and D. Colson, Phys. Rev. Lett. **110**, 167002 (2013).

[27] M. D. Watson, T. K. Kim, A. A. Haghighirad, N. R. Davies, A. McCollam, A. Narayanan, S. F. Blake, Y. L. Chen, S. Ghannadzadeh, A. J. Schofield, M. Hoesch, C. Meingast, T. Wolf, and A. I. Coldea, Phys. Rev. B **91**, 155106 (2015).

[28] V. Brouet, M. F. Jensen, P.-H. Lin, A. Taleb-Ibrahimi, P. Le Fèvre, F. Bertran, C.-H. Lin, W. Ku, A. Forget, and D. Colson, Phys. Rev. B **86**, 075123 (2012).

[29] S. Blundell and D. Thouless, Am. J. Phys. **71**, 94 (2003).

[30] S. Shen, W. Zhong, D. Li, Z. Lin, Z. Wang, X. Gu, and S. Feng, Inorganic Chem. Commun. **103**, 25 (2019).

[31] Y. Li, Z. Yin, Z. Liu, W. Wang, Z. Xu, Y. Song, L. Tian, Y. Huang, D. Shen, D. L. Abernathy, J. L. Niedziela, R. A. Ewings, T. G. Perring, D. M. Pajerowski, M. Matsuda, P. Bourges, E.

Mechthild, Y. Su, and P. Dai, Phys. Rev. Lett. **122**, 117204 (2019).

[32] A. Subedi, L. Zhang, D. J. Singh, and M. H. Du, Phys. Rev. B **78**, 134514 (2008).

[33] S. Graser, A. F. Kemper, T. A. Maier, H.-P. Cheng, P. J. Hirschfeld, and D. J. Scalapino, Phys. Rev. B **81**, 214503 (2010).

[34] J.-H. Chu, J. G. Analytis, K. De Greve, P. L. McMahon, Z. Islam, Y. Yamamoto, and I. R. Fisher, Science **329**, 824 (2010).

[35] J.-H. Chu, H.-H. Kuo, J. G. Analytis, and I. R. Fisher, Science **337**, 710 (2012).

[36] R. M. Fernandes, A. V. Chubukov, and J. Schmalian, Nat. Phys. **10**, 97 (2014).

[37] G. Liu, H. Liu, L. Zhao, W. Zhang, X. Jia, J. Meng, X. Dong, J. Zhang, G. F. Chen, G. Wang, Y. Zhou, Y. Zhu, X. Wang, Z. Xu, C. Chen, and X. J. Zhou, Phys. Rev. B **80**, 134519 (2009).

[38] K. Nakayama, Y. Miyata, G. N. Phan, T. Sato, Y. Tanabe, T. Urata, K. Tanigaki, and T. Takahashi, Phys. Rev. Lett. **113**, 237001 (2014).

[39] T. Qian, X.-P. Wang, W.-C. Jin, P. Zhang, P. Richard, G. Xu, X. Dai, Z. Fang, J.-G. Guo, X.-L. Chen, and H. Ding, Phys. Rev. Lett. **106**, 187001 (2011).

[40] L. Zhao *et al.*, Nat. Commun. **7**, 10608 (2016).

[41] X. H. Niu, R. Peng, H. C. Xu, Y. J. Yan, J. Jiang, D. F. Xu, T. L. Yu, Q. Song, Z. C. Huang, Y. X. Wang, B. P. Xie, X. F. Lu, N. Z. Wang, X. H. Chen, Z. Sun, and D. L. Feng, Phys. Rev. B **92**, 060504(R) (2015).

[42] D. Liu *et al.*, Nat. Commun. **3**, 931 (2012).

[43] S. Tan, Y. Zhang, M. Xia, Z. Ye, F. Chen, X. Xie, R. Peng, D. Xu, Q. Fan, H. Xu, J. Jiang, T. Zhang, X. Lai, T. Xiang, J. Hu, B. Xie, and D. Feng, Nat. Mater. **12**, 634 (2013).

[44] J. J. Lee, F. T. Schmitt, R. G. Moore, S. Johnston, Y.-T. Cui, W. Li, M. Yi, Z. K. Liu, M. Hashimoto, Y. Zhang, D. H. Lu, T. P. Devereaux, D.-H. Lee, and Z.-X. Shen, Nature (London) **515**, 245 (2014).

[45] Q. Song, T. L. Yu, X. Lou, B. P. Xie, H. C. Xu, C. H. P. Wen, Q. Yao, S. Y. Zhang, X. T. Zhu, J. D. Guo, R. Peng, and D. L. Feng, Nat. Commun. **10**, 758 (2019).

[46] V. Bannikov, I. Shein, and A. Ivanovskii, Phys. B (Amsterdam, Neth.) **407**, 271 (2012).

[47] D. G. Quirinale, V. K. Anand, M. G. Kim, A. Pandey, A. Huq, P. W. Stephens, T. W. Heitmann, A. Kreyssig, R. J. McQueeney, D. C. Johnston, and A. I. Goldman, Phys. Rev. B **88**, 174420 (2013).

[48] Y. Li, Z. Liu, Z. Xu, Y. Song, Y. Huang, D. Shen, N. Ma, A. Li, S. Chi, M. Frontzek, H. Cao, Q. Huang, W. Wang, Y. Xie, R. Zhang, Y. Rong, W. A. Shelton, D. P. Young, J. F. DiTusa, and P. Dai, Phys. Rev. B **100**, 094446 (2019).